JACS
JOURNAL OF THE AMERICAN CHEMICAL SOCIETY
Article
pubs.acs.org/JACS

Increased Back-Bonding Explains Step-Edge Reactivity and Particle Size Effect for CO Activation on Ru Nanoparticles

Lucas Foppa, Christophe Copéret, and Aleix Comas-Vives*

Department of Chemistry and Applied Biosciences, ETH Zürich, Vladimir Prelog Weg 1-5, CH-8093 Zürich, Switzerland

Supporting Information

ABSTRACT: Carbon monoxide is a ubiquitous molecule, a key feedstock and intermediate in chemical processes. Its adsorption and activation, typically carried out on metallic nanoparticles (NPs), are strongly dependent on the particle size. In particular, small NPs, which in principle contain more corner and step-edge atoms, are surprisingly less reactive than larger ones. Hereby, first-principles calculations on explicit Ru NP models (1−2 nm) show that both small and large NPs can present step-edge sites (e.g., B_5 and B_6 sites). However, such sites display strong particle-size-dependent reactivity because of very subtle differences in local chemical bonding. State-of-the-art crystal orbital Hamilton population analysis allows a detailed molecular orbital picture of adsorbed CO on step-edges, which can be classified as *flat* (η^1 coordination) and *concave* (η^2 coordination) sites. Our analysis shows that the CO π-metal d_π hybrid band responsible for the electron back-donation is better represented by an oxygen lone pair on flat sites, whereas it is delocalized on both C and O atoms on concave sites, increasing the back-bonding on these sites compared to flat step-edges or low-index surface sites. The bonding analysis also rationalizes why CO cleavage is easier on step-edge sites of large NPs compared to small ones irrespective of the site geometry. The lower reactivity of small NPs is due to the smaller extent of the Ru−O interaction in the η^2 adsorption mode, which destabilizes the η^2 transition-state structure for CO direct cleavage. Our findings provide a molecular understanding of the reactivity of CO on NPs, which is consistent with the observed particle size effect.

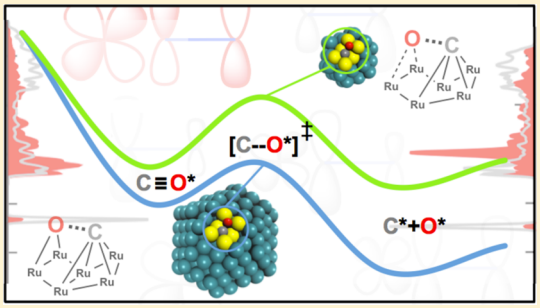

1. INTRODUCTION

The adsorption and activation of carbon monoxide are elementary steps occurring on the surface of transition-metal nanoparticle (NP) catalysts during important chemical processes such as the water−gas shift reaction (WGS)[1,2] and the Fischer−Tropsch synthesis (FTS).[3−7] CO bonding to metal surfaces or NPs can be described with the Blyholder model, inspired by frontier molecular orbital (MO) theory in molecular chemistry.[8] According to this model, the interaction between the adsorbed CO molecule and the metallic surface atoms is the result of electron donation (to the metal) and back-donation (from the metal) via the 5σ and $2\pi^*$ MOs (HOMO and LUMO, respectively, Figure 1a), analogous to metal−carbonyl bonding in molecular complexes.[9] However, it was shown more recently that only the formation of CO−*d*-metal hybrid bands by means of perturbation theory can account for CO electron density distribution as determined by spectroscopy,[10,11] raising the need for more-detailed theoretical descriptions of CO adsorption on metal catalysts, such as the $\sigma-\pi$ model[10] and the attraction−repulsion mechanism.[12,13]

So far, CO−metal bonding models concentrated on flat surface low-index sites (hcp, fcc, top). However, real catalyst NPs present a large variety of sites beyond terraces of flat surfaces, such as step-edge and kinks (Figure 1b). Additionally, NPs have a finite character (NP size) that influences the coordination of metal atoms and therefore their interaction with adsorbates, such as CO.[14] The electronic structure of CO adsorbed on other types of sites than flat surfaces as well as the dependence of σ and π contributions to the bonding strength on such sites is thus not clearly understood.

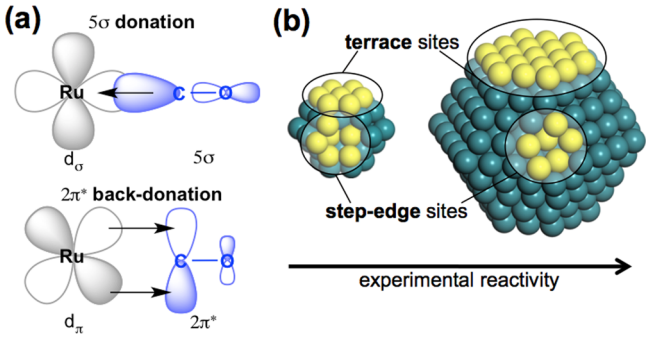

Figure 1. (a) Blyholder model for CO adsorption on Ru surface sites. (b) Different types of terrace and step-edge sites on metal NPs (marked in yellow) of different sizes and experimental NP size effect on reactivity.

Understanding the bonding on step-edge sites is important since they are proposed to be the active sites for the direct cleavage of the strong C≡O bond (bond energy equal to 1072

Received: August 19, 2016
Published: November 30, 2016

DOI: 10.1021/jacs.6b08697
J. Am. Chem. Soc. 2016, 138, 16655−16668

kJ mol^{-1}; for comparison, the value for C−C is equal to 346 kJ mol^{-1})[9] according to both experimental[15−17] and theoretical studies.[16,18−26] First introduced by Hardeveld and Montfoort in the 1960s,[27−29] B_5 sites are among the most studied step-edge sites, and they have been suggested to play a key role also for the case of N_2 cleavage or alkyne semi-hydrogenation.[21,30−34] Regarding CO activation, it is known that small NPs are less reactive toward FTS than large ones.[6,35] This particle size effect is often ascribed to the lack of B_5 sites on small NPs,[33,36,37] although it has also been rationalized by alternative activation routes involving H_2, which would assist the CO activation step.[38]

Among transition-metal catalysts, Ru NPs are a very appealing model system to understand the bonding and reactivity of CO, since Ru is highly active in the conversion of CO/H_2 to long-chain hydrocarbons (FTS) and in the WGS. Experimental studies as well as theoretical treatments through density functional theory (DFT) calculations on Ru slab surface models agree in that CO activation occurs on Ru step-edge B_5 as well as B_6 sites of corrugates/open surfaces with much lower activation energies (50−90 kJ mol^{-1}) compared to flat surfaces (227 kJ mol^{-1}).[17,20,23−25,39] Ru catalysts also display a particle size effect, i.e., a marked decrease in reactivity per surface atom for small Ru NP catalysts (ca. 1−2 nm) compared to larger ones (>10 nm), for instance in FTS.[35,36]

Here, we use first-principles calculations on explicit Ru NP models with realistic sizes in combination with a crystal orbital Hamilton population (COHP) bonding analysis to investigate the electronic structure of CO adsorbed in Ru step-edge sites. We use a MO interpretation of its band structure and show why step-edge sites are more reactive toward CO activation than flat surfaces and how the particle size effect can be understood from the electronic structure rather than from only the abundance of step-edge sites, as proposed so far.

2. COMPUTATIONAL DETAILS

Periodic DFT calculations were carried out with Vienna Ab Initio Simulation Package (VASP) code,[40−42] using a plane-wave basis set with pseudopotentials (PAW method) and the Perdew−Burke−Ernzerhof (PBE) exchange-correlation functional.[43,44] Two different Ru NP models (Figure 2) of 1 and 2 nm diameter size were considered, as well as slab Ru surface models for comparison.

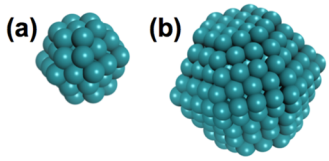

Figure 2. Initial Ru NP models used in this work: (a) Ru_{57} and (b) Ru_{323} NPs.

Regarding the bonding analysis, from the plane-wave calculated electron density, we partitioned the band-structure energy in terms of local orbital-pair contributions within the COHP analysis.[45−47] This approach is analogous to the crystal orbital overlap population (COOP) analysis developed by Hoffmann in the context of extended Hückel calculations,[48,49] the goal of which is to extract chemical bonding information out of a DFT calculation, e.g., bonding and antibonding character of the electronic states. Further details on the computational methods are described in the Supporting Information (SI).

3. RESULTS

3.1. Stability of Defects on Ru NPs. The starting Ru hexagonal close-packed (hcp) NP models expose only (001) and (101) surface terminations. However, other surface terminations and defects are found in real NP catalysts.[50] In order to understand the most likely formed additional surface terminations/defects in Ru NPs, we evaluated the energy of NP structures formed by removal of different combinations of one, two, and three atoms from the Ru_{57} cluster, forming Ru_{56}, Ru_{55} and Ru_{54} NPs (Table S1 and Figure 3a.1). As expected, the most stable structures are obtained by removing the less saturated atoms on the edge (5*b*/7/5c or 5*a*/6/5b) or the corners (2*b*/3a/5a) of the NP (Table S1). The cohesive energy is proportional to the surface/volume ratio ($\sim N^{-1/3}$) and decreases (in magnitude) with decreasing number of NP atoms.

Analyzing the structures of the defect-containing NPs (Ru_{55} and Ru_{54}, Figure 3a.2), we observe that several of the metal surface arrangements created display structures similar to those present on (104), (100), and (111) extended surfaces. Moreover, some of the Ru NPs containing these sites are more stable compared to other possible structures with the same number of atoms, in special B_5 $(104)_{2\text{-}1\text{-}2}$ and B_5 $(104)_{2\text{-}2\text{-}1}$ sites in the Ru_{55} series and B_5 $(100)_A$, B_6 (111), and B_6 $(100)_B$ sites in the Ru_{54} series (Figure 3a.2). From now on, the sites are labeled B_n, where *n* is the number of metal atoms that are in close contact to an adsorbed species to the site (Hardeveld and Montfoort notation).[29] We also indicate the surface termination that contains such sites. B_5 (104) sites are labeled either "2-1-2" or "2-2-1" since they are analogous to sites on both $(104)_A$ and $(104)_B$ extended surfaces.

Due to the computational cost of calculations with the Ru_{323} NP model, we used the features observed for Ru_{57} NPs and analyze the formation of only the analogous most stable sites on the Ru_{323} NP. Figure 3b.1 shows the structure and stability of such sites on Ru_{323}. Compared to the smaller NP, the difference in cohesive energy among the defect-containing Ru_{323} NP structures is much smaller (ca. 1 vs 10 kJ mol^{-1} for Ru_{57}), since the excess of energy created by the generation of more unsaturated atoms in the defects is averaged over a larger number of atoms for the Ru_{323} NP.

In the case of Ru_{323}, three or five atoms were removed from the original structure to form defects. For the Ru_{320} series of NPs, we observe that B_6 (111) and B_5 $(104)_{2\text{-}1\text{-}2}$ defects are more stable compared to B_5 $(104)_{2\text{-}2\text{-}1}$. For Ru_{318} NPs, B_5 $(100)_A$ site is preferred over B_5 $(100)_B$. In fact, the formation of the most stable defects on Ru_{323} can be seen as the appearance of new surface terminations on the original particle (Figure 3b.2), which contained originally only (001) and (101) low-energy surfaces. Indeed, $(104)_A$, $(100)_A$, and (111) terminations appear in the Wulff construction of a Ru hcp NP (6/*mmm* point group) generated with DFT-derived surface energies (Figure 3b.3). The following terminations were considered (ordered by increasing surface energy): (001), $(104)_A$, $(100)_A$, $(101)_A$, $(104)_B$, $(201)_A$, $(102)_A$, $(102)_B$, (111), $(210)_A$, $(210)_B$, $(201)_B$, $(101)_B$, and $(100)_B$ (respective surface energy values are shown in Table S2). The Wulff construction represents the NP equilibrium shape of relative large structures (>3 nm), for which the NP edge and corner energies are negligible with respect to the size of the facets.

From our calculations of the explicit NPs, the B_5 and B_6 step-edge sites are among the most stable defects that can be formed in both Ru_{57} (ca. 1 nm) and Ru_{323} (ca. 2 nm). The formation of

DOI: 10.1021/jacs.6b08697
J. Am. Chem. Soc. 2016, 138, 16655−16668

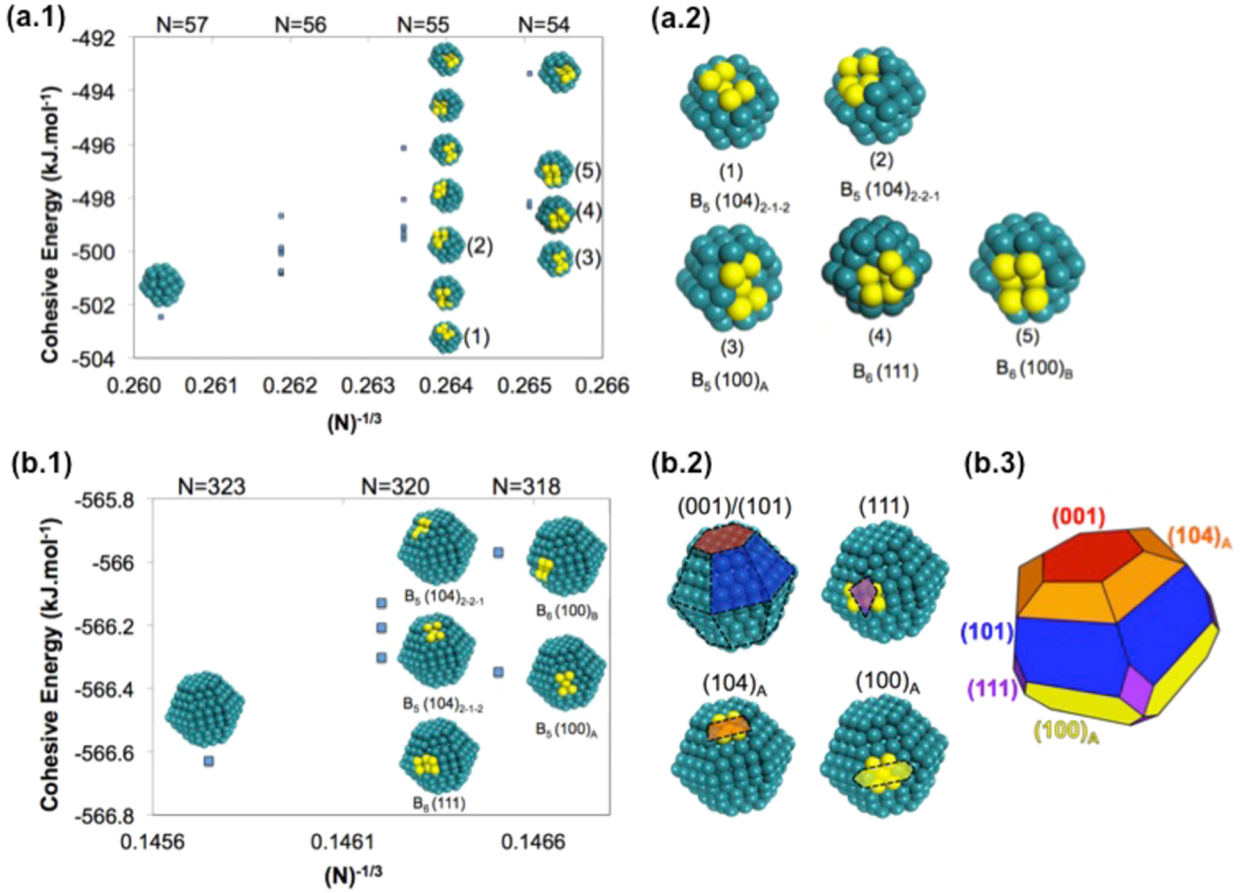

Figure 3. (a.1) Structure of defects formed from the Ru_{57} model and corresponding cohesive energy (in kJ mol^{-1}) as a function of $N^{-1/3}$, N being the number of atoms of the nanoparticle. (a.2) Detailed structures for selected defects. (b.1) Structure of defects formed from the Ru_{323} model and corresponding cohesive energy (in kJ mol^{-1}) as a function of $N^{-1/3}$, N being the number of atoms of the nanoparticle. (b.2) Most stable defects that originate new surface terminations on Ru_{323}. (b.3) Wulff construction of a Ru hcp NP.

step-edges for Ru_{57} and Ru_{323} NPs is always associated with an energy cost, consistent with their presence as defects. The energy cost to form a B_5 site on Ru_{57} and Ru_{323} NPs is +56 and +43 kJ mol^{-1}, respectively (details of the calculations provided in SI). B_5 sites are therefore only slightly more probable on Ru_{323} compared to Ru_{57} (within 10 kJ mol^{-1}), as recently found on Co NPs (2.9 nm diameter) by molecular dynamics simulations.[51] This is in contrast to the previous assumption that B_5 sites are only possible for larger Ru NPs (>2 nm).[29] It should be noted that particles in real catalysts are constructed from a finite fixed number of metal atoms originally coming from the precursor (e.g., metal salt) that do not freely diffuse across the support. Therefore, it is reasonable to assume that, in spite of the cost to form defects, a distribution of particles with different numbers of atoms (and sizes) will present them.

We then investigate the geometry and coordination environment of step-edge sites formed in both small and large Ru NPs and their ability to activate CO.

3.2. CO Adsorption. *3.2.1. CO Adsorption on Extended Surfaces.* On the most stable flat surface (001), carbon monoxide is preferentially adsorbed on a top site with an adsorption energy of −187 kJ mol^{-1}, calculated with the PBE exchange-correlation functional. This value corresponds to an overestimation of the adsorption energy of ca. 20 kJ mol^{-1} compared to experiment (zero-point energy (ZPE) excluded),[52] which shows that PBE is a good compromise between cost and accuracy, since it allows evaluating large systems such as Ru_{323} NPs with a fairly good description. On the Ru (001) surface, CO adsorption energy on bridge, fcc, and hcp sites takes values equal to −165, −167, and −176 kJ mol^{-1}, respectively, according to our calculations.

CO adsorption energy values and bond lengths for each of the sites considered in our analysis can be found in Table S3. The optimized structures of adsorbed CO on the different surfaces models are available in the SI and shown in Figures 7 and S2−S6. Multiple adsorption strengths are found depending on the type of site, reflecting the diversity of CO adsorption modes on Ru surface sites. CO adsorption energies are found within the range from −125 to −205 kJ mol^{-1}. CO binding to step-edge sites can be either weaker (e.g., $B_6(111)$ site, −125 kJ mol^{-1}) or stronger (e.g., B_6 $(100)_B$ site, −205 kJ mol^{-1}) than on the flat (001) surface (−187 kJ mol^{-1}).

Nevertheless, our calculations show that not only the geometry of the Ru site dictates CO adsorption but also its coordination. For instance, the sites B_5 $(104)_{2\text{-}1\text{-}2}$ and B_5 $(104)_{2\text{-}2\text{-}1}$ are present on both the $(104)_A$ or $(104)_B$ extended surface terminations, but with different coordination environments, as depicted in Figure 4. CO adsorbs (μ_2-η^1 geometry, see Figure S3) on the B_5 $(104)_{2\text{-}1\text{-}2}$ site of the $(104)_B$ surface (CN = 7, 7, 11, 7, 7, Figure 4b) with an adsorption energy equal to −181 kJ mol^{-1}. On the $(104)_A$ surface B_5 $(104)_{2\text{-}1\text{-}2}$ site (CN = 7, 7, 11, 9, 9, Figure 4a), which has the same geometry but is more saturated, the CO adsorption strength is much lower and the adsorption energy is equal to −143 kJ mol^{-1} (μ_3-

DOI: 10.1021/jacs.6b08697
J. Am. Chem. Soc. 2016, 138, 16655−16668

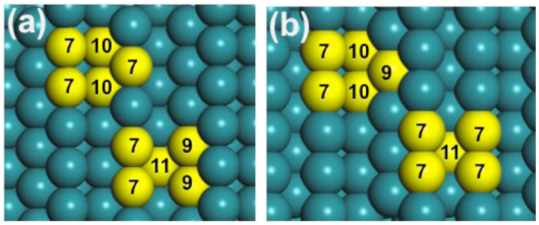

Figure 4. B_5 sites present on (a) $(104)_A$ and (b) $(104)_B$ surfaces (in yellow). The numbers in the figure show the CN of the Ru surface atoms.

η^1 geometry). The stronger metal−CO bond for the less-saturated $B_5(104)_{2\text{-}1\text{-}2}$ site can be understood from the bond order conservation (BOC) principle: unsaturated metal atoms bind more strongly to CO in order to compensate their lower CN compared to the stable bulk metal, for which CN = 12.

However, for the case of the B_5 $(104)_{2\text{-}2\text{-}1}$ site on (104) surfaces (μ_3-η^2 geometry in both cases, see Figure 4 and S4), CO binds much more strongly for the site containing more-saturated Ru atoms (CN = 7, 9, and 10) on the $(104)_B$ surface (−208 kJ mol^{-1}) (Figure 4b) compared to the less-saturated site present on the $(104)_A$ surface (−164 kJ mol^{-1}) (Figure 4a). As it will be discussed in section 3.4.3, the origin of this unusual trend can only be understood in terms of the electronic structure.

If CO adsorption properties depend not only on the type of site considered, but also on the coordination of the metallic atoms, we may wonder what happens for Ru NP models of various sizes.

3.2.2. CO Adsorption on Ru NPs. Figure 5 shows the CO adsorption energies and C−O bond lengths for the sites

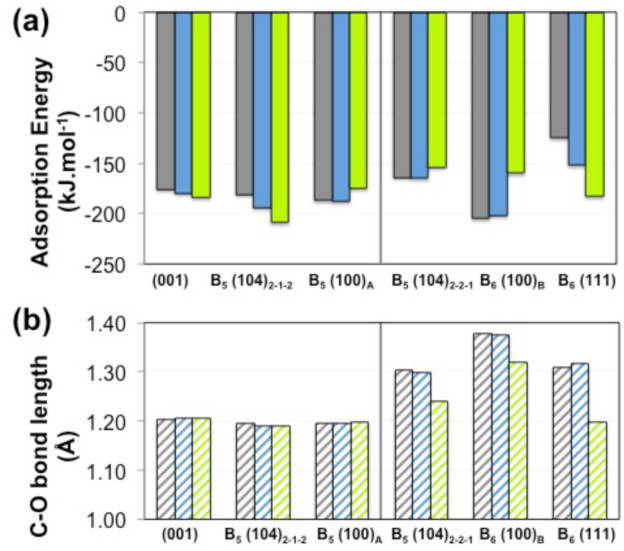

Figure 5. (a) CO adsorption energy and (b) adsorbed C−O bond distance on Ru extended surfaces and NPs. Gray, extended surface; blue, Ru_{323}; green, Ru_{57}. The C−O distance on the free CO is equal to 1.13 Å for the free molecule calculated at the same level of theory.

considered in this study and located on Ru_{323} and Ru_{57} NP models (section 3.1). The values for sites with the same geometry on extended surfaces are shown for comparison. Note that only the less saturated versions of the two possible B_5 sites on the (104) extended surfaces (*vide supra*) are considered here. This is because the saturation (i.e., CNs) of B_5 sites on NPs (Figures 3a.2 and 3b.1) is closer to that of the less saturated sites of the extended surfaces.

For a given site, we observe a decrease in the coordination of the metal atoms (CNs are given in Table S3) when going from the Ru_{323} to the Ru_{57} particle. By carefully analyzing CO adsorption geometries (Figures 7 and S2−S6) on the different sites considered, we can generally distinguish two types of CO adsorption modes that relate to the tendencies of adsorption strength and bond length shown in Figure 5.

(a) For some of the sites, CO adsorbs normal to the surface in an η^1 fashion (Scheme 1a) and *higher* CO−metal binding

Scheme 1. Coordination Modes of the CO Molecule on the Different Ru Sites: (a) η^1 and (b) η^2 Types

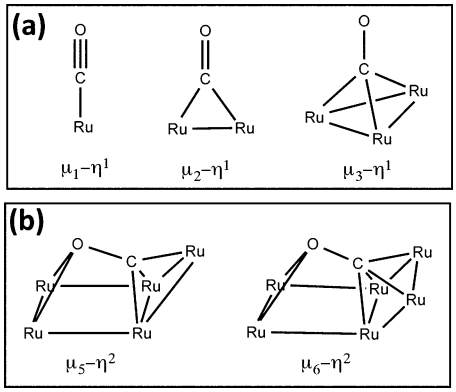

strengths are obtained for the small Ru_{57} NPs compared to Ru_{323} (panel a and entries 1−7 of Table S3), while the C−O bond of the adsorbed molecule is equal to ca. 1.2 Å irrespective of the site coordination (panel b). This is the case for hcp (001), B_5 $(104)_{2\text{-}1\text{-}2}$, and B_5 $(100)_A$ sites, which will be called from now on *flat* sites.

(b) For other sites, CO adsorption occurs in a tilted η^2 configuration (Scheme 1b) and CO−metal adsorption strength is lower on the Ru_{57} system than on Ru_{323}. (panel a and entries 11−17 of Table S3). In this case, however, C−O distances of the adsorbed molecule can be as large as 1.4 Å and always decrease for the small NPs (panel b). This is the case for B_5 $(104)_{2\text{-}2\text{-}1}$, B_6 $(100)_B$, and B_6 (111) sites, which we will call *concave* sites.

The high stability of CO on an η^2 adsorption with more-saturated atoms in a *concave* site is counterintuitive, since unsaturated metal atoms are expected to bind more strongly to CO according to the bond order conservation principle. This η^2 CO coordination to metal sites is similar to what has been reported on molecular Ru organometallic cluster analogues, $Ru_6(\eta^2\text{-}\mu_4\text{-CO})_2(CO)_{13}(\eta^6\text{-}C_6Me_6)$[53] or $Ru_6(\mu_3\text{-H})(\eta^2\text{-}\mu_4\text{-CO})_2(CO)_{13}(\eta^5\text{-}C_5H_4Me)$,[54] whose structures have been determined from X-ray crystallography.

C−O stretching frequencies calculated with DFT (Table S5) lie in the range of 1750−1960 cm^{-1} for *flat* sites, whereas they are much lower for concave sites (918−1142 cm^{-1}). In the case of the B_6 $(100)_B$ site, for instance, the C−O bond length reaches an extremely elongated distance equal to 1.38 Å for the most coordinated site on the extended surface. The corresponding calculated C−O bond stretching frequency on this site is equal to 918 cm^{-1}. Interestingly, some early experimental data from the 1980s describe unusually low CO stretching frequencies (range 1065−1245 cm^{-1}) upon adsorption on Mo (100),[55] Fe (100),[56] Cr (110),[57] and K-

DOI: 10.1021/jacs.6b08697
J. Am. Chem. Soc. 2016, 138, 16655−16668

modified Ru (001) single-crystal surfaces,[58] which were assigned, at that time, to a "tilted precursor for the CO dissociation".[56] Also, flat-lying CO molecules chemisorbed to a Cu (311) step-edged surface were identified by angle-resolved photoemission spectroscopy.[59]

It should be noted that B_5 $(100)_A$ and B_6 (111) do not follow the overall NP-size-dependent CO adsorption trend observed within flat and concave types of sites, respectively (Figure 5a); i.e., for B_5 $(100)_A$ the adsorption strength decreases for the site on the small NP and for B_6 (111) it increases. This is because, for these two sites, there is a change in the CO adsorption geometry according to the system on which the site is located. For instance, CO adsorbs with a μ_6-η^2 geometry on the B_6 (111) site of the extended surface and on Ru_{323}, but μ_2-η^1 on the Ru_{57} NPs (Figure S6). Therefore, instead of a decrease in the adsorption strength as it would be expected for a concave site, a higher binding with C−O bond length equal to 1.2 Å is observed for the less saturated B_6 (111) site on Ru_{57}.

3.3. CO Activation. *3.3.1. Low Coverage: CO Activation Energy Trend.* Next, we evaluated carbon monoxide dissociation through a direct pathway. The activation energy values for each of the sites are shown in Table S3 and Figure 6.

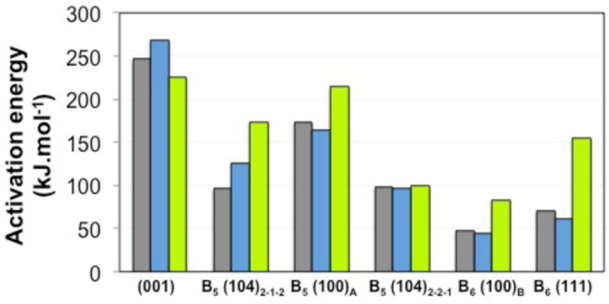

Figure 6. Activation energy for CO direct dissociation on Ru extended surfaces and NPs. All activation energy values are referenced to the corresponding CO adsorbed state: $E_{act} = E_{TS} - E_{IS}$, where E is the electronic energy in kJ mol^{-1}. Gray, extended surface; blue, Ru_{323}; green, Ru_{57}.

Transition-state (TS) optimized structures for the different sites can be found in Figures 7 and S2−S6. We define the activation energy as the difference between the TS (electronic) energy and the energy of the precursor structure where CO is adsorbed (IS).

We first observe that the energy barriers for all the step-edge sites considered here (extended surface sites) are much lower (174 to 47 kJ mol^{-1}) compared to that of the (001) extended surface (247 kJ mol^{-1}), especially for the concave sites. Therefore, not only B_5 sites from (104) surfaces, typically used to model the reactivity of step-edge sites, are able to activate CO with low energy barriers, but also other types of sites, such as B_6 with $(100)_B$ and (111) surface geometries.[23,39] This difference in reactivity was previously ascribed to (i) the enhanced back-donation from Ru to antibonding CO orbitals of the adsorbed molecule on step-edge sites and (ii) the greater stability of dissociated C* and O* fragments on step-edge sites, as a thermodynamic factor which influences the kinetics.[30]

Comparing the activation energy within each type of step-edge site, we observe that CO splitting typically presents similar barriers on a Ru_{323} NP or on an extended surface site, whereas it is surprisingly more energy demanding on the small Ru_{57} NP sites for all of the evaluated metal ensembles (Figure 6). The more difficult CO activation on smaller clusters is consistent with what has been shown for Rh and Fe NPs by previous DFT studies.[60,61] While for some sites little energy barrier differences are found for different NP sizes—e.g., B_5 $(104)_{2\text{-}1\text{-}1}$, range 96–100 kJ mol^{-1} (entries 11−14 of Table S3)—others present significant differences in the energy barriers. In the case of the B_6 (111) site, for instance, the activation barrier is equal to 71 kJ mol^{-1} on an extended surface vs 61 kJ mol^{-1} and 155 kJ mol^{-1} on Ru_{323} and Ru_{57} (entries 18−20 of Table S3), respectively, representing an energy difference between the most and the least active systems of 94 kJ mol^{-1}. The more difficult CO activation on smaller NPs is consistent with the observed decrease of rate in CO activation during FTS for smaller NPs, even though the size range considered here is small compared to those investigated experimentally.[35]

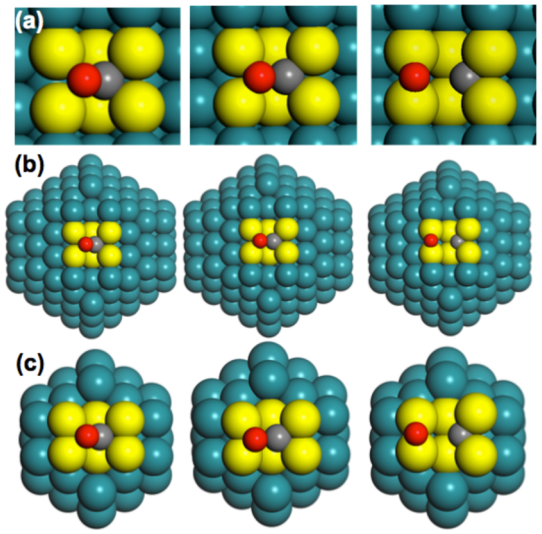

Figure 7. Optimized structures for adsorbed CO (left), transition state (TS) for CO direct splitting (middle), and dissociated C* and O* atoms (right) on the B_6 $(100)_B$ site in different systems: (a) $(100)_B$ extended surface, (b) Ru_{323} NP, and (c) Ru_{57} NP.

In order to understand why the direct CO cleavage energy barriers are higher for the less saturated sites of the small NP, we compared the energy diagrams for CO splitting on each of the sites considered on either Ru_{57}, Ru_{323}, or periodic extended surfaces (Figure 8). Since the activation energy is the difference between the TS structure and the adsorbed CO molecule energies, both (i) strong CO adsorption and (ii) lack of TS stabilization are factors that increase the energy barrier to form C* and O* from CO*.

The increased CO adsorption strength on flat sites—as well as B_6 (111), which presents CO η^1 adsorption on Ru_{57}—of the small NP indeed contributes to increase the activation energy for CO dissociation, especially in the case of B_5 $(104)_{2\text{-}1\text{-}2}$ and B_6 (111) sites (see Figure 8b,f). However, the increase in adsorption energy for these sites on Ru_{57} with respect to Ru_{323} (equal to 15 and 33 kJ mol^{-1} for B_5 $(104)_{2\text{-}1\text{-}2}$ and B_6 (111), respectively) itself does not explain the larger difference in activation energy (47 and 94 kJ mol^{-1} for B_5 $(104)_{2\text{-}1\text{-}2}$ and B_6 (111), respectively). Moreover, the difference in adsorption strength is not important for the remaining flat sites. For concave sites, since small NPs have lower CO adsorption energies, we should expect an even lower activation energy for

DOI: 10.1021/jacs.6b08697
J. Am. Chem. Soc. 2016, 138, 16655−16668

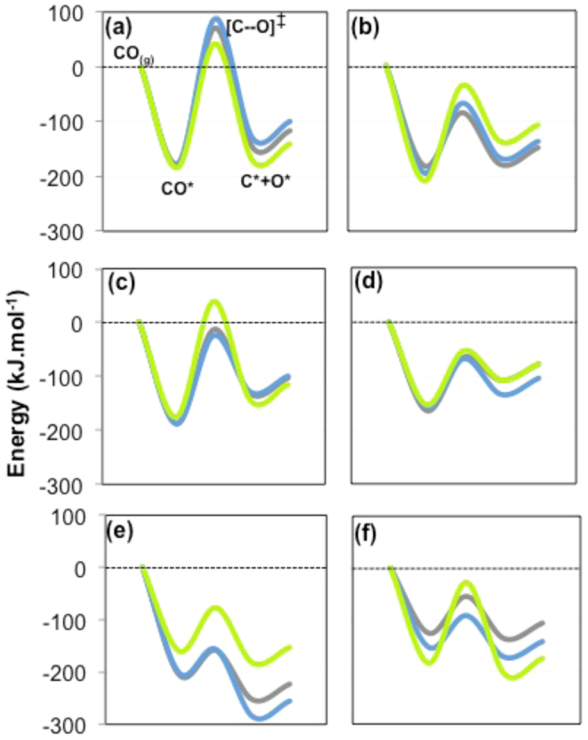

Figure 8. Energy profiles (electronic energy) for the CO dissociation on (a) (001) hcp, (b) B_5 $(104)_{2\text{-}1\text{-}2}$, (c) B_5 $(100)_A$, (d) B_5 $(104)_{2\text{-}2\text{-}1}$, (e) B_6 $(100)_B$, and (f) B_6 (111). The energies are referenced to the corresponding clean surface (or NP) and the gas-phase CO molecule. Gray, extended surface; blue, Ru_{323}; green, Ru_{57}.

the CO dissociation (section 3.2), in contrast to what is obtained here.

So as to verify whether the thermodynamics of CO splitting influences the energy barriers for this reaction, we plotted the activation energy as a function of the reaction energy values (Brønsted–Evans–Polanyi (BEP) plot) for the different systems considered in this study (Ru_{57}, Ru_{323}, and extended surfaces), shown in Figure S7. The BEP plots are shown separately per type of step-edge site. First, the BEP plots evidence that only 6-fold (B_6) sites are able to dissociate CO exoenergetically, irrespective of the particle size. This shows that the stabilization of adsorbed C* on 4-fold sites is significantly higher than in the 3-fold sites (B_5 sites), once O* is, for all the cases, located in a bridge site. Indeed, C* species are ca. 60 kJ mol^{-1} more stabilized in the 4-fold position of the B_5 $(104)_{2\text{-}2\text{-}1}$ site compared to the 3-fold position of the same site. The increased stabilization of adsorbed carbon on 4-fold sites forming reconstructed square-planar aromatic structures has been previously reported for Ni and Co.[62]

Regarding the linear BEP relationship, expected to be valid within each type of site, the points corresponding to the sites on Ru_{57} are for most of the cases out of the linear trend that is displayed by Ru_{323} NPs and extended surfaces step-edge sites (Figure S7). Much higher barriers are observed for the smaller particle than what is expected from the reaction energy. Particularly on the B_5 $(100)_A$ and B_6 (111) sites (entries 8–10 and 18–20 of Table S3), where although the CO activation is more exoenergetic on Ru_{57} compared to Ru_{323} or the periodic extended surfaces, the energy barriers are much higher for the smaller NPs. The higher stability in the CO dissociation product (C* and O*) on the Ru_{57} compared to the Ru_{323} NP system is likely due to the enhanced curvature of the Ru_{57} NPs, which increases the C–O distance on the dissociated state and thus reduces the repulsive interaction between the products C* and O*. For instance, in the case of the B_5 $(100)_A$ site, the C–O distances of C*+O* activation products on Ru_{323} and Ru_{57} are equal to 3.47 and 4.06 Å, respectively (3.58 and 4.17 Å for B_6 (111) site).

In conclusion, neither the adsorption strength nor the reaction thermodynamics can account for the more difficult CO activation on smaller Ru NPs as calculated by DFT. The reason for this behavior must then be linked to the lower stability of the TS on Ru_{57} compared to Ru_{323} or the extended surface itself, which will be further analyzed in detail in section 3.4.

3.3.2. High Coverage. During the course of reactions involving CO activation, the surface of the catalyst is covered with a significant amount of CO molecules. This is the case for FTS, whose reactants are CO and H_2. Since CO adsorption strength is much stronger than H_2 adsorption on Ru (ca. 180 vs 40 kJ mol^{-1} on the (001) surface), CO is the main surface species. Previous contributions have shown that, under FTS reaction conditions, the CO coverage on Ru NPs, defined as the number of CO molecules per surface metallic atom, lies in the range of 1.0–1.5 monolayer (ML).[38,50,63] In particular, we recently used a combined experimental–theoretical DFT approach to evaluate CO chemisorption on Ru hcp NPs supported on SiO_2.[50] Such high CO coverages are expected during FTS in real catalysts due to the high pressures (up to 50 bar) typically employed in this reaction.[4]

Hence, we also have evaluated CO direct splitting under high coverage conditions (ca. 1.0 ML) on Ru_{323} NP step-edge sites. This model was chosen because (i) it is representative of nanometric size NPs, (ii) the step-edges of Ru_{323} are more reactive than those present on Ru_{57} (section 3.3.1) and finally (iii) the curvature of the NP allows a higher CO coverage than on periodic extended surfaces.

Table 1 shows the calculated CO adsorption, activation, and reaction energy values for CO direct cleavage on different sites of a CO-covered Ru_{323} NP model (for details of the calculations, see computational details section of the SI). The optimized structures of adsorbed CO, TSs, and dissociated states under high CO coverage are depicted in Figure 9. For all the step-edge sites considered, the adsorption energy decreases compared to low coverage conditions (compare adsorption energy values in Table 1 to Table S3), due to the repulsion of neighboring molecules. Interestingly, CO displays a very weak binding to B_6 (111) site at such high coverages, with an adsorption energy of only −43 kJ mol^{-1} (Table 1, Entry 5), which is comparable to reported values for CO adsorption under high coverage at NPs terraces (−42 kJ mol^{-1}).[38] The low adsorption strength reported here for this specific site contrasts with the common assumption that step-edges are blocked by strongly adsorbed CO moieties during reactive conditions. Indeed, the other step-edge sites considered bind CO rather strongly, with adsorption energy values ranging from −184 to −109 kJ mol^{-1} (Table 1, entries 1–4).

The CO activation causes an increase in the number of adsorbed species; i.e., the surface coverage increases after CO dissociation since two species (adsorbed C* and O*) are formed from only one (the adsorbed CO). At such high coverage, there is a strong repulsion between the C* and O* and the neighboring CO molecules, and for that reason all the reaction energies are significantly less favored than at low CO coverage. For example, the CO dissociation on B_6 sites

DOI: 10.1021/jacs.6b08697
J. Am. Chem. Soc. 2016, 138, 16655–16668

Table 1. Energetics of the CO Adsorption and Direct Dissociation on Ru_{323} NP Step-Edge Sites at ca. 1.0 ML CO Coverage

entry	site type	E_{ads} (kJ mol^{-1})	E_{act} (kJ mol^{-1})	ΔE_{react} (kJ mol^{-1})
1	B_5 $(104)_{2\text{-}1\text{-}2}$	−140	219	180
2	B_5 $(100)_A$	−154	250	212
3	B_5 $(104)_{2\text{-}2\text{-}1}$	−109	151	124
4	B_6 $(100)_B$	−184	117	112
5	B_6 (111)	−43	122	115

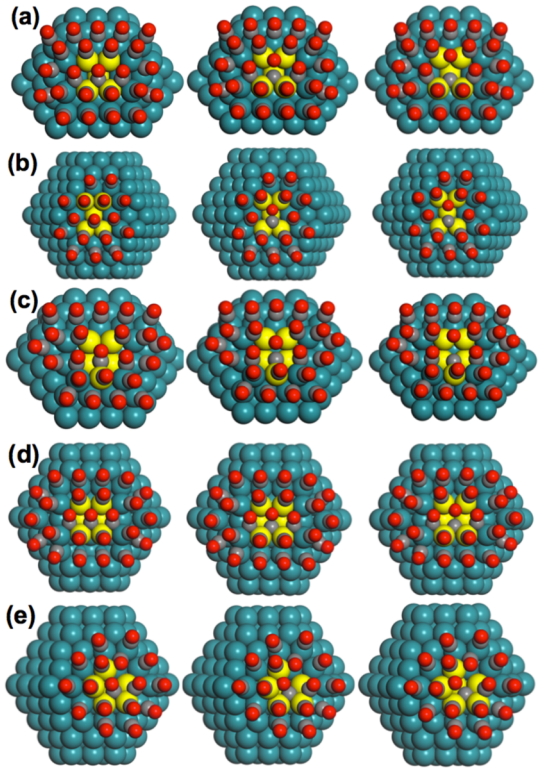

Figure 9. Optimized structures for adsorbed CO (left), transition state (TS) for CO direct splitting (middle), and dissociated C* and O* atoms (right) on the (a) $B_5(104)_{2\text{-}1\text{-}2}$, (b) B_5 $(100)_A$, (c) B_5 $(104)_{2\text{-}2\text{-}1}$, (d) B_6 $(100)_B$, and (e) B_6 (111) sites at ca. 1 ML CO coverage. The metal atoms composing the site are shown in yellow.

experiences a shift from exoenergetic (entries 16 and 19 of Table S3) to endoenergetic (entries 4 and 5 of Table 1) when going from low to high CO surface coverage. For the specific case of B_5 sites, there is also a significantly more endoenergetic character when going from low to high coverage.

Activation energy values are also significantly increased compared to CO low coverage conditions due to repulsion at the TS. However, the increase is much more pronounced for the flat step-edge sites than for concave ones. Therefore, flat sites experience a sharp decrease of reactivity toward CO direct activation with increasing CO coverage, with higher activation energies equal to 219 and 250 kJ mol^{-1}. On the other hand, the concave B_5 $(104)_{2\text{-}2\text{-}1}$, B_6 (111), and B_6 $(100)_B$ sites are still able to directly activate CO with affordable energy barriers at high coverage, with activation energies of 151, 122, and 117 kJ mol^{-1}, respectively (see Table 1).

The CO activation process at high coverage as calculated here assumes the migration of spectator CO molecules around the step-edge site to accommodate the newly formed C* and O* species. In previous DFT studies,[38] CO direct splitting on a Ru_{201} NP B_5 $(104)_{2\text{-}1\text{-}2}$ site at high CO coverage (1.55 ML) was evaluated considering separately the energy cost of forming a vacancy prior to reaction (119 kJ mol^{-1}) plus the intrinsic barrier for the activation of another CO molecule on the "local low coverage" step-edge (150 kJ mol^{-1}), giving rise to a global energetic cost of 269 kJ mol^{-1}.

Our results for this specific B_5 $(104)_{2\text{-}1\text{-}2}$ site suggest that, at least from an energetic point of view, the migration of CO molecules in the proximity of the step-edge site during CO cleavage is more favorable (energy barrier of 219 kJ mol^{-1} for cleavage with migration) than the pathway with prior CO desorption (estimated as 140 kJ mol^{-1} (desorption) + 126 kJ mol^{-1} (activation at low coverage) = 262 kJ mol^{-1}). It should be noted that C−O bond cleavage may also occur from hydrogenated intermediates produced by reaction with adsorbed hydrogen on the NPs terraces during FTS,[38] which is consistent with the reaction rate law typically showing a dependence on the H_2 pressure. The hydrogen-assisted CO activation route via the HCOH* intermediate on a Ru_{201} NP terrace covered with 1.55 ML CO, for instance, is less energy demanding (165 kJ mol^{-1}) than the direct cleavage on the B_5-type site (269 kJ mol^{-1}) according to DFT calculations reported elswhere.[38] Similarly, water and alkyl chains, also present on the catalyst surface during FTS, were also suggested to assist CO bond cleavage.[64,65] Since terraces are relatively less abundant on smaller particles, hydrogen-assisted pathways are also consistent with the particle size effect on FTS.

Comparing the energetics for CO direct activation on the step-edge sites of Ru_{323} described in this work with that of reported hydrogen-assisted routes on Ru_{201} NP terraces at 1.55 ML coverages (165 kJ mol^{-1}),[38] i.e., both at realistic CO coverage, we see that direct CO activation on any of the concave sites evaluated—B_5 $(104)_{2\text{-}2\text{-}1}$ (151 kJ mol^{-1}), B_6 $(100)_B$ (117 kJ mol^{-1}), and B_6 (111) (122 kJ mol^{-1})—presents more-affordable energy barriers, which supports the proposal that step-edge sites are the active sites for CO activation. If this is the case, then the CO activation rate dependence on NP size could be explained not only on the basis of the abundance of step-edge sites discussed so far in the literature, but also on the different reactivity of unsaturated step-edge sites of small transition-metal Ru NPs as reported here. In any case, bimolecular CO activation pathways cannot be discarded in the context of FTS,[66] and most likely both direct and assisted CO dissociation process are competitive, as suggested by recent experimental investigations.[37]

3.4. Bonding Analysis. As described in sections 3.2 and 3.3, the trends in CO adsorption and cleavage on step-edge sites with respect to NP size cannot be understood by simply comparing the energy and geometry of the adsorbed species. We thus applied a COHP analysis to our electronic structure calculations in order to evaluate the CO internal bond as well as the CO−metal site interactions on the basis of a chemically intuitive molecular approach.[47] The COHP analysis describes the bonding, nonbonding, and antibonding character of the interaction of a selected pair of atoms by partitioning the DFT-generated band-structure energy in terms of orbital-pair contributions. Since our calculations are based on the Projected Augmented Wave (PAW) method, which uses a set of (nonlocalized) plane waves as basis set, a projection scheme is needed beforehand, leading to the projected COHP (pCOHP) curve.[46] The pCOHP quantity is generally represented as −(pCOHP), so that positive and negative

DOI: 10.1021/jacs.6b08697
J. Am. Chem. Soc. 2016, 138, 16655−16668

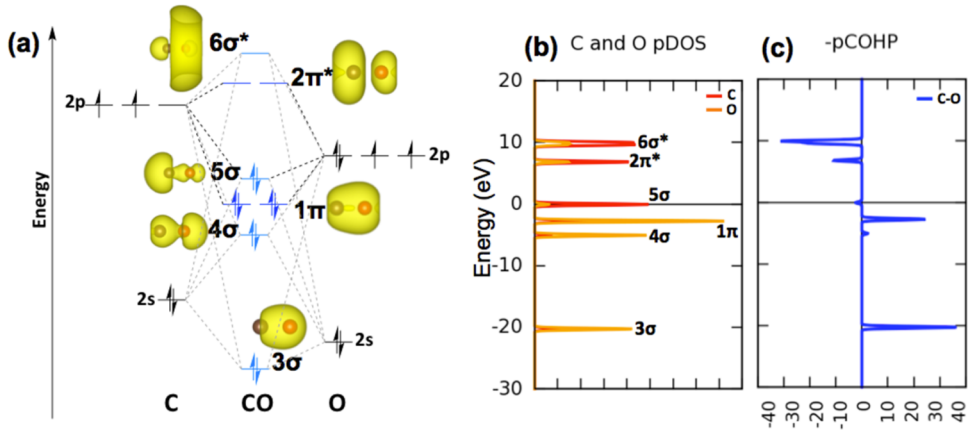

Figure 10. (a) CO MO diagram with respective electron isodensity surfaces representing each MO. (b) DOS and (c) pCOHP curves calculated with the same level of theory of this work.

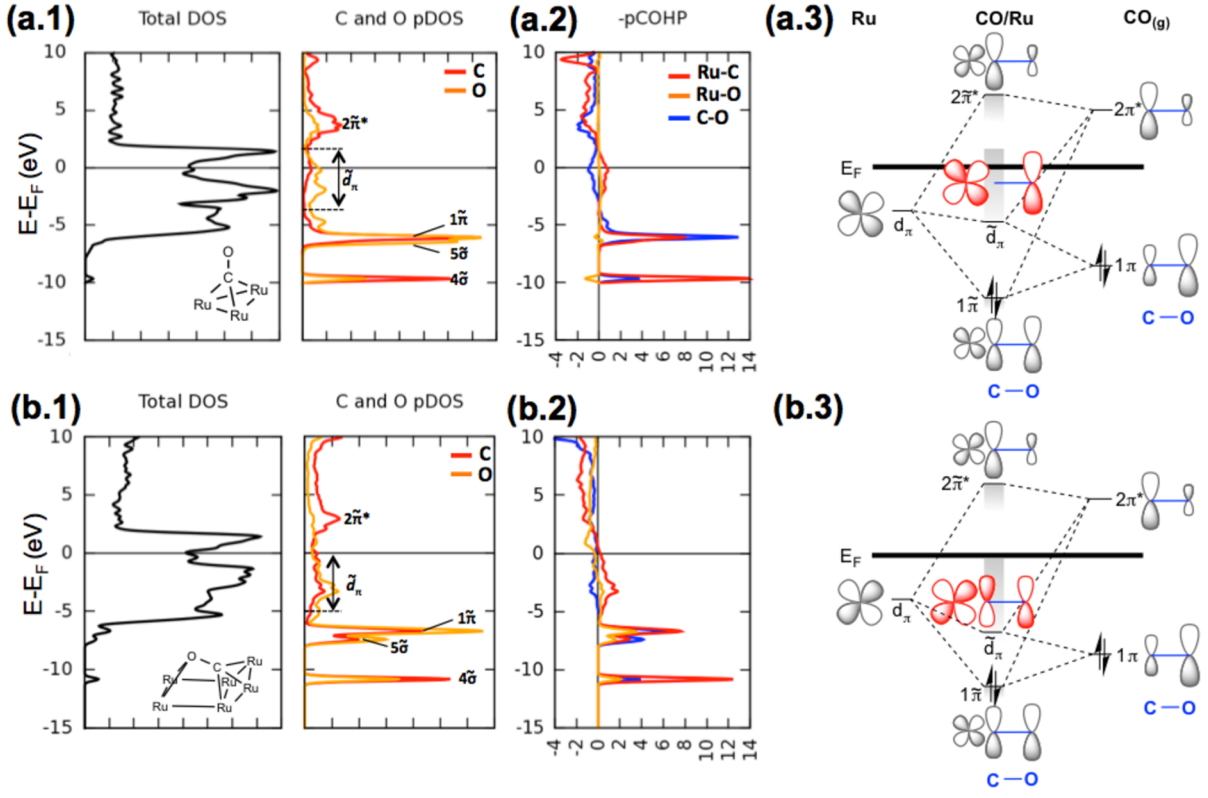

Figure 11. (a.1) DOS and (a.2) pCOHP curves for CO adsorption on (001) hcp site (extended surface). (a.3) Schematic representation of π-interactions on a hcp site. Adapted from ref 10. The DOS and pCOHP curves as well as the schematic representation of π-interactions for B_6 $(100)_B$ site (extended surface) are shown in (b.1), (b.2), and (b.3), respectively.

values correspond, respectively, to bonding and antibonding states.

We will start our analysis by considering the isolated CO molecule. The CO molecular orbital diagram together with the electron density isosurfaces corresponding to the MOs and the carbon/oxygen projected density of states (pDOS) are depicted in Figure 10a,b. The pCOHP curve for the C−O pair generated from a periodic calculation is shown in Figure 10c. From the pCOHP analysis of CO, most of the bonding contributions on the C−O bond come from the 3σ and 1π orbitals, which, according to the pDOS curves, are both polarized toward the oxygen atom. The 4σ and 5σ MOs are only slightly involved in the bonding and can be therefore primarily assigned to the oxygen and carbon lone pairs of CO Lewis structure, respectively, in view of their larger contribution on the oxygen and carbon CO atoms, respectively (see pDOS curve in Figure 10b).

3.4.1. CO Adsorption on a Flat Site. In the following, we briefly describe the electronic structure of CO adsorbed as an η^1 species on a flat (001) hcp site. This analysis is used as a benchmark, since the electronic structure of CO adsorbed to such sites has been extensively studied and is well understood, for example, for the cases of flat Ni or Pt surfaces.[10,13,67] A more detailed description is provided in the SI. We refer to donation and back-donation concepts to explain CO bonding to the metal (Blyholder model), which are standard in molecular

DOI: 10.1021/jacs.6b08697
J. Am. Chem. Soc. 2016, 138, 16655−16668

chemistry, even though rehybridization models are common in the literature and needed to explain CO MO mixing with each other upon adsorption.[10,11]

Upon CO adsorption to the (001) hcp flat site, CO MOs rehybridize with metal bands and with one another (within the CO molecule) and transform into rather delocalized bands, named as the "tilde" of the original MOs, as shown in Figure 11a.1. Especially interesting for our analysis is the formation of the $\tilde{d}_\pi$ band from the mixing of the metal d_π band with 1π and $2\pi^*$ MOs, which is exclusively located around the oxygen atom as a "lone pair". From the pCOHP analysis (Figure 11a.2), we see that, within the CO molecule itself (C−O pair, blue line), the bonding contributions come from the $4\tilde{\sigma}$, $5\tilde{\sigma}$ (σ-bonding) and $1\tilde{\pi}$ (π-bonding) bands, while $\tilde{d}_\pi$ and $2\tilde{\pi}^*$ bands are antibonding. Regarding Ru−C interactions (CO binding to the metallic surface site, red line), all these bands are bonding, with the exception of $2\tilde{\pi}^*$, which is also the only nonpopulated band above the Fermi level.

Figure 11a.3 displays a "MO diagram" schematically representing the CO π interaction with the (001) hcp site described by the pCOHP analysis above and adapted from ref 10. For the sake of clarity, only one Ru atom and one d orbital are represented. The diagram shows how the 1π orbital is stabilized upon CO adsorption, which relates to its polarization toward the carbon atom. The $\tilde{d}_\pi$ band (oxygen lone pair) is only slightly shifted down in energy and remains spread below and above the Fermi level. The population of the $\tilde{d}_\pi$ band which is not present on the free molecule has two effects: (i) it is responsible for the weakening of C−O bond and red shifts C−O stretching frequencies with respect to the gas phase (antibonding C−O), which corresponds to the electron back-donation from the metal to CO, and (ii) it contributes to CO binding to the surface (bonding C−Ru), which stabilizes the system.

3.4.2. CO Adsorption on a Concave Site. We now turn our attention to CO adsorption on the concave B_6 $(100)_B$ site of the extended surface. For this site, $4\tilde{\sigma}$, $5\tilde{\sigma}$, and $1\tilde{\pi}$ states can be identified as narrow bands in the C and O pDOS (Figure 11b.1), respectively, at approximately −11.0, −7.5, and −6.5 eV with respect to the E_F, analogous to the case of the flat site. The broad $\tilde{d}_\pi$ and $2\tilde{\pi}^*$ bands are also present in the range from −4 to 0 eV and around +3 eV, respectively.

The features observed for the σ system on the (001) hcp site are also present for the B_6 $(100)_B$ site, namely the electron redistribution between C and O on the $5\tilde{\sigma}$ band. Additionally, $5\tilde{\sigma}$ is even more stabilized than $1\tilde{\pi}$ on the concave site compared to the flat one (see the splitting of the two $5\tilde{\sigma}$ and $1\tilde{\pi}$ narrow bands in Figure 11b.1 compared to Figure 11a.1), which indicates higher CO−metal σ bonding. However, the most remarkable differences between CO adsorption on flat and concave site concern the π interactions.

Although $1\tilde{\pi}$ and $2\tilde{\pi}^*$ bands present similar characteristics for both types of sites, $\tilde{d}_\pi$ can no longer be regarded as an oxygen lone pair for the case of CO η^2 adsorption on B_6 $(100)_B$ site, in contrast to the case of the η^1 adsorption on (001) hcp. This is because the $\tilde{d}_\pi$ band has components on both C and O for the case of the concave site, as observed in the decomposition of the pDOS (Figure 11b.1). As a consequence of electron delocalization of this $\tilde{d}_\pi$ band within C and O, its position is shifted down with respect to the Fermi level on the concave site. Whereas $\tilde{d}_\pi$ has components 1 eV above the Fermi level on the (001) hcp site, it is completely below E_F for B_6 $(100)_B$ (compare Figures 11a.1 and 11a.2), which impacts the bonding patterns.

Inspection of the pCOHP curves for the B_6 $(100)_B$ site (Figure 11b.2) shows an increase in the electron density back-donation from the metal to the molecule when compared to (001) hcp site, since the $\tilde{d}_\pi$ antibonding band is completely filled in the B_6 $(100)_B$ site, resulting in a significant weakening of the C−O bond (blue line). Similar to the case of the flat site, the $\tilde{d}_\pi$ is Ru−C bonding (red line), but in this case most of the band is filled with bonding contributions owing to a stronger Ru−C bond than for the flat sites.

Another important difference in the pCOHP bonding pattern between the two types of sites concerns Ru−O interactions. In the case of the (001) hcp site, Ru−O interactions are slightly nonbonding, whereas they are strongly bonding for the B_6 $(100)_B$ site (compare Figures 11a.2 and 11b.2, orange line), as expected from the distance between the O and the Ru surface atoms (3.06 and 2.2 Å for (001) hcp and B_6 $(100)_B$ sites, respectively). This means that, apart from carbon, oxygen's interaction with the surface also contributes to the bonding of CO to the metal site.

In order to understand the Ru−O interactions on the B_6 $(100)_B$ site, we compared the orbital-decomposed C and O pDOS curves corresponding to the CO molecule adsorbed on the (001) hcp flat and on the B_6 $(100)_B$ concave sites (Figure 12). While C and O p_x and p_y orbitals (z is taken along the C−O bond axis) are degenerated in the case of CO adsorption on the (001) hcp site according to the projection scheme (Figure 12a), they are not equivalent for the B_6 $(100)_B$ site (see Figure 12b). The main difference is that, in the concave site, the p_y orbital of the oxygen atom (shown in green in Figure 12) presents components not only in the energy range of the π bands ($1\tilde{\pi}$, $\tilde{d}_\pi$, and $2\tilde{\pi}^*$) like for the (001) hcp site, but also in the energy range of the $4\tilde{\sigma}$ band. This indicates that the $4\tilde{\sigma}$ band, which is exclusively located on the C−O bond axis (z) for the case of the (001) hcp site, is extended toward the Ru−O bond axis, forming a Ru−C−O−Ru $4\tilde{\sigma}$ bonding band on the B_6

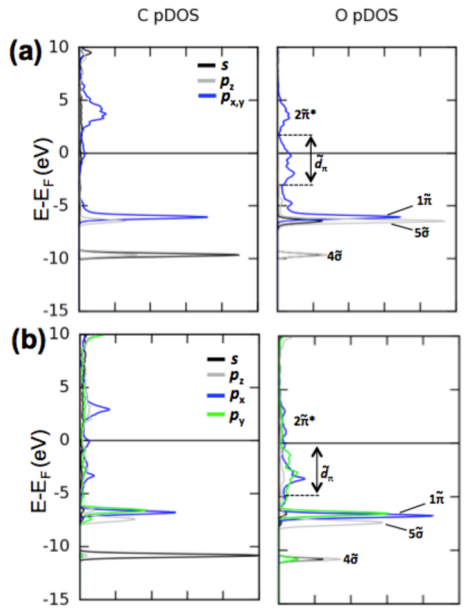

Figure 12. Orbital-projected carbon and oxygen DOS for CO adsorption on (a) (001) hcp and (b) B_6 $(100)_B$ sites on extended surfaces.

DOI: 10.1021/jacs.6b08697
J. Am. Chem. Soc. 2016, 138, 16655−16668

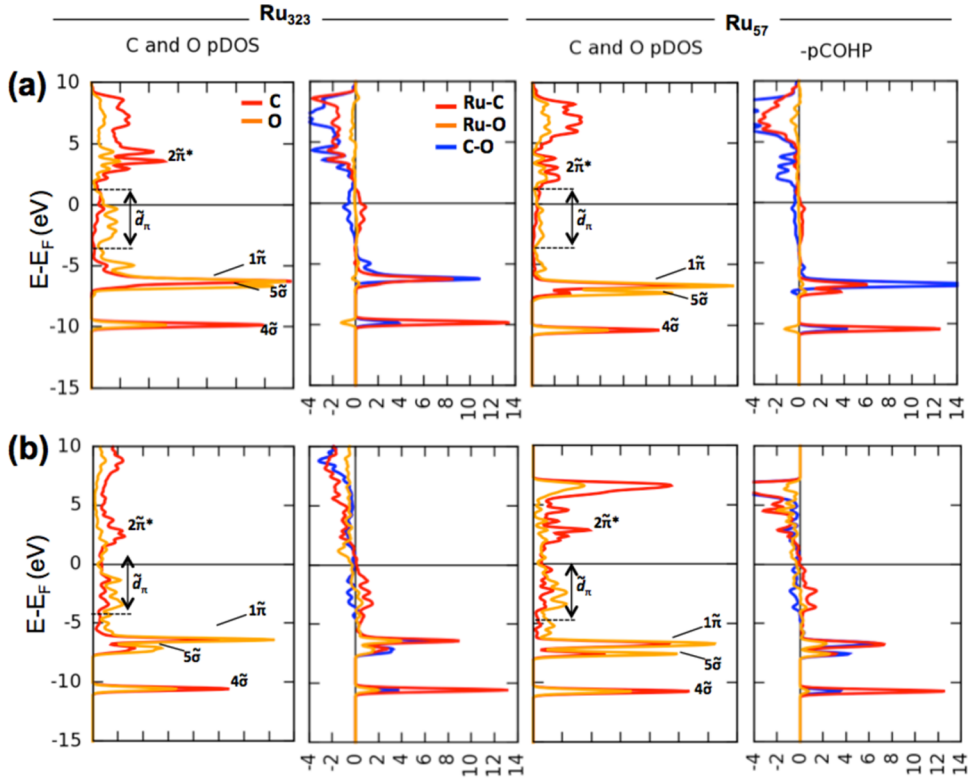

Figure 13. DOS and pCOHP curves for CO adsorption on (a) (001) hcp and (b) B_6 $(100)_B$ sites in Ru_{323} and Ru_{57} NPs.

$(100)_B$ site. The pCOHP Ru−O curve (Figure 11b.2) shows that the bonding character comes mainly from $4\tilde{\sigma}$ and $1\tilde{\pi}$ interactions, meaning that the CO π system is also involved in the Ru−O bonding.

A rather simple picture to understand CO bonding to the B_6 $(100)_B$ site is to consider that the oxygen lone pair present in a hypothetical η^1 CO adsorption geometry on a concave site ($\tilde{d}_\pi$ band, equivalent to a molecular LUMO) forms a new σ Ru−O bond with unoccupied metal d states of neighboring Ru atoms (HOMO) that tilt the molecule to an η^2 configuration. As a consequence, part of the electron density is shifted from the oxygen atom to the Ru−O bond axis, delocalizing the $\tilde{d}_\pi$ band over the CO molecule and stabilizing the system. Decomposition of the Ru−O pCOHP curve for the three Ru atoms on the B_6 $(100)_B$ site (Figure S8) shows that, indeed, mostly the two Ru atoms in closer proximity to the oxygen atom participate in the Ru−O bond.

With all the previous information in hand, we propose a revised "MO diagram" view of CO π bonding to a metal site upon an η^2 configuration, shown in Figure 11b.3. In this simplified picture of the CO adsorption to the B_6 $(100)_B$ site, we see that, while $1\tilde{\pi}$ and $2\tilde{\pi}^*$ bands present rather similar shape compared to the case of the (001) hcp site (Figure 11a.3), the $\tilde{d}_\pi$ band is now spread along the carbon and oxygen atoms of the CO molecule and lies completely below the Fermi level. Since the CO bonding to the metal surface is a combination of σ donation and π back-donation contributions, the latter is much more important for the concave site and has, as consequence, both C−O elongation (from 1.20 Å on (001) hcp to 1.38 Å on B_6 $(100)_B$) and higher adsorption strength (−176 to −208 kJ mol^{-1}) compared to the flat (001) hcp site.

The pDOS/pCOHP analysis of CO adsorption on the remaining sites on extended surfaces (Figure S9) shows that the conclusions derived for (001) hcp and B_6 $(100)_B$ sites are actually general and can be extended to all flat and concave sites considered in this work, respectively. Nonetheless, the remaining question is why there are different CO adsorption behaviors for flat and concave sites with respect to the NP size.

3.4.3. NP Size Dependence of CO Adsorption. In order to understand how the interplay of σ donation and π back-donation effects on the different CO coordination modes affects CO's adsorption and bond length for the different particle sizes (Figure 5a), we also evaluated DOS and pCOHP curves for the adsorption on (001) hcp and B_6 $(100)_B$ sites in Ru_{323} and Ru_{57} (Figure 13). For both sites on Ru_{323}, the electronic structure and bonding are very similar to those described for the site on an extended surface (Figures 11), which is translated on the similar adsorption energy values and bond lengths for both cases (Figure 5a and b). Nevertheless, for both sites on the small Ru_{57}, which are less saturated, important differences are observed.

For the (001) hcp flat site, decreasing the particle size from Ru_{323} to Ru_{57} causes a better stabilization of the $5\tilde{\sigma}$ band relative to $1\tilde{\pi}$ (compare the two pDOS curves in Figure 13a) and a decrease in the electron back-donation ($\tilde{d}_\pi$ band becomes less intense). The (slight) increase in the adsorption strength (adsorption energy changes from −180 to −184 kJ mol^{-1} on Ru_{323} and Ru_{57} (001) hcp sites, respectively) can thus be ascribed to stronger σ bonding on the less saturated site, an effect is in line with what one expects from the bond order conservation principle. The adsorption energy value for the (001) hcp site on an extended surface is equal to −176 kJ mol^{-1}. It should be noted that π back-donation occurs in both small and large particles for the (001) hcp flat sites, which is evidenced by the C−O bond length of 1.21 Å, larger than that of the free CO (1.13 Å). However, as explained above, this effect has a limited influence in dictating CO adsorption proprieties for the case of flat sites, as opposed to concave ones.

DOI: 10.1021/jacs.6b08697
J. Am. Chem. Soc. 2016, 138, 16655−16668

In the B_6 $(100)_B$ concave site, the $5\tilde{\sigma}$ bonding contributions retain the same energy range with respect to $1\tilde{\pi}$ when going from the site on Ru_{323} to Ru_{57} (Figure 13b). However, the Ru−O interactions and the π system are significantly modified when changing the particle size. Ru−O bonding interactions all drop in intensity compared to other components of the pCOHP curve, especially in the case of $4\tilde{\sigma}$ and $1\tilde{\pi}$ bands. Accordingly, the $\tilde{d}_\pi$ band becomes less intense for the smaller particle, which indicates a reduced electron back-donation for the site on Ru_{57}. Therefore, because of the lack of Ru−O stabilization and electron back-donation, which play important roles for CO bonding to this type of site, the adsorption strength sharply drops from an adsorption energy of −202 kJ mol^{-1} on Ru_{323} to −160 kJ mol^{-1} on Ru_{57} for the B_6 $(100)_B$ site. The smaller extent of electron back-donation is confirmed by the C−O bond length, which decreases from 1.38 to 1.32 Å when going from the Ru_{323} to the Ru_{57} NP. The extent of back-donation can also rationalize the stronger CO adsorption strength to the concave $B_5(104)_{2\text{-}2\text{-}1}$ site of the $(104)_B$ surface (more saturated, d_{C-O} = 1.31 Å) compared to that of the $(104)_A$ surface (less saturated, d_{C-O} = 1.30 Å), as exposed in Figure 4.

In order to obtain further quantitative evidence of the NP size dependence of the electron back-donation, we also evaluated the evolution of C and O charges from the CO free molecule to CO adsorption on the different sites of extended surfaces compared to Ru_{57} NP. The electron density transfer from the metal to the π system of the molecule (back-donation) has an effect of equilibrating the lack of electron density on the carbon atom of the CO molecule, which has partially given away its 5σ electron lone pair to the metal. The carbon charge can thus serve as an indication of the balance between σ donation and the extent of electron back-donation.

The atom partitioning of the electron density (Bader charge (q_B) analysis, shown in Table 2) shows that C is electron-deficient (q_B = +1.2 e) in the free CO, with −1.2 e on the oxygen atom (Table 2, entry 1). Upon CO adsorption, the oxygen remains negatively charged, with a charge comparable to that of the free molecule (q_B range from −1.1 to −0.9 e), while the electron density around the carbon atom increases significantly.

Table 2. Bader Charge (q_B) Analysis of Adsorbed CO

		$q_{B,C}$ (e)		$q_{B,O}$ (e)	
entry	site type	surface	Ru_{57}	surface	Ru_{57}
1	–	+1.20[a]		−1.20[a]	
2	hcp (001)	+0.46	+0.49	−0.91	−0.98
3	B_5 $(104)_{2\text{-}1\text{-}2}$	+0.69	+0.62	−1.02	−1.03
4	B_5 $(100)_A$	+0.61	+0.62	−1.02	−1.04
5	B_5 $(104)_{2\text{-}2\text{-}1}$	+0.26	+0.48	−1.02	−1.08
6	B_6 $(100)_B$	0.00	+0.23	−1.00	−1.04
7	B_6 (111)	+0.24	+0.68	−1.02	−1.06

[a]Free CO.

By comparing flat and concave sites on extended surfaces, we see that carbon is much less electron deficient for the latters (q_B from 0 to +0.26 e, entries 5−7 of Table 2) than for the formers (q_B from +0.46 to +0.69 e, entries 2−4 of Table 2). This is in agreement with the higher stability and population of the delocalized $\tilde{d}_\pi$ bands on concave sites with respect to flat ones, as discussed above on the basis of the electronic structure. The CO η^2 adsorption on the B_6 $(100)_B$ site is the most extreme case, since the strong electron back-donation completely equilibrates the carbon atom electron deficiency to a Bader charge value of zero. Not surprisingly, this site is also the one for which CO presents the highest adsorption strength among all the evaluated step-edge sites (adsorption energy value of −208 kJ mol^{-1}).

3.4.4. Transition State for CO Dissociation. Can we also understand CO activation NP size dependence from the electronic structure and Bader charges? Since the stability of the TS for direct CO dissociation on step-edge sites was identified as the main factor causing the higher energy barriers on Ru_{57} compared to Ru_{323} (section 3.3.1), we analyzed the electronic structure of the TS on the flat hcp (001) and concave B_6 $(100)_B$ site on the extended surface as well as on Ru_{323} and Ru_{57} systems. The case of the (001) hcp site is treated separately in the SI, since the TS structure for this site contains the oxygen in a top position that is unique among all the sites studied here. We start our analysis by considering the CO dissociation TS for the B_6 $(100)_B$ site on the extended surface.

The pDOS and pCOHP curves corresponding to the TS for CO dissociation on the B_6 $(100)_B$ site of the extended surface are shown in Figure 14a. The electronic structure of the TS no longer resembles that of the adsorbed CO. The C−O distance on this TS is equal to 1.89 Å, indeed pointing to a late, more product-like TS. Two sharp bands appear in the C and O pDOS curves around the energy values of −12 and −18 eV

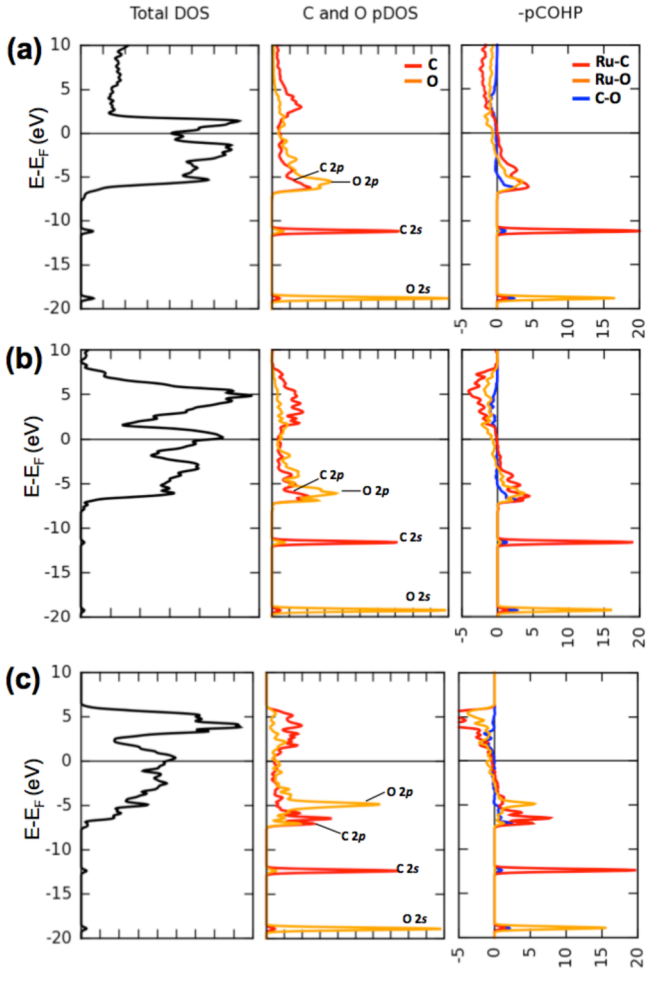

Figure 14. DOS and pCOHP curves for CO direct dissociation TS on B_6 $(100)_B$ in (a) the extended surface, (b) Ru_{323}, and (c) Ru_{57} NPs.

DOI: 10.1021/jacs.6b08697
J. Am. Chem. Soc. 2016, 138, 16655−16668

with respect to the Fermi level, which correspond to the 2*s* carbon and oxygen orbitals, respectively. Additionally, a broad feature relative to C and O *p* orbitals mixed with metal *d*-bands is observed above −7 eV. According to the pCOHP analysis, some occupied bands are still bonding with respect to C−O, meaning that C and O still interact on the TS despite the large C−O distance. Those are mainly located in the energy range of C and O *p* orbitals. Regarding Ru−O and Ru−C interactions, they present bonding contributions, which are below E_F and thus occupied.

3.4.5. NP Size Dependence of CO Activation. By comparing the electronic structure of the TS for CO dissociation on the B_6 $(100)_B$ of the extended surface (Figure 14a) to that on a site on the Ru_{323} NPs (Figure 14b), the same patterns are observed. Nevertheless, the TS for CO cleavage on the B_6 $(100)_B$ site of the Ru_{57} NPs (Figure 14c) presents major differences by comparison with the two former ones. We see that the center of the oxygen *p* states mixed with metal bands is higher in energy in the case of Ru_{57} compared to Ru_{323}, whereas bands associated with carbon *p* orbitals lie in the same energy range. The fact that O 2*p* band is higher in energy in the TS suggests that the Ru−O bonding is weaker for the site on the small NPs. The smaller extent of the Ru−O interactions seems thus responsible for the weaker stabilization of the CO dissociation TS and consequentially for the higher activation energy in the B_6 $(100)_B$ site of the Ru_{57} (83 kJ mol^{-1}) when compared to Ru_{323} (45 kJ mol^{-1}) and the extended surface (47 kJ mol^{-1}). The role of the M−O bond in facilitating CO dissociation on step-edges was also pointed out as the reason for the increased reactivity of Fe-promoted Rh B_5 sites in a recent DFT study.[68]

The weaker Ru−O interaction for the TS of CO dissociation on the B_6 $(100)_B$ site of the small Ru NPs compared to the larger ones is similar to the effect previously discussed, which explained the decrease of the CO adsorption strength on concave sites when going from the Ru_{323} to the Ru_{57} NPs. In the case of CO adsorption, the weaker oxygen binding to the surface decreased the electron back-donation and also the charge density on the CO carbon atom. Bader charge analysis for the TS structures on the B_6 $(100)_B$ site located both on the extended surface and on Ru_{57} (entry 5 of Table 3) also shows that the carbon atom of the TS structure is surrounded by more electron density in the case of the surface (q_B = −0.48 e) as opposed to the small NPs (q_B = −0.38 e), even though it is no longer possible to identify the bands involved in the electron back-donation as for the case of an adsorbed CO molecule.

Table 3. Bader Charge (q_B) Analysis of CO Dissociation TS Structures

		$q_{B,C}$ (e)		$q_{B,O}$ (e)	
entry	site type[a]	surface	Ru_{57}	surface	Ru_{57}
1	hcp (001)	−0.40	−0.38	−0.60	−0.67
2	B_5 $(104)_{2-1-2}$	−0.39	−0.38	−0.76	−0.73
3	B_5 $(100)_A$	−0.33	−0.29	−0.74	−0.74
4	B_5 $(104)_{2-2-1}$	−0.38	−0.40	−0.73	−0.72
5	B_6 $(100)_B$	−0.48	−0.38	−0.78	−0.73
6	B_6 (111)	−0.41	−0.34	−0.73	−0.73

Inspection of the Bader charges on the TS structures of the remaining concave step-edge sites evaluated in this work (Table 3) shows that the carbon charge can also be used to understand the intensity of the Ru−O interaction and thus the reactivity toward CO activation for these sites. For the B_6 (111) concave site, carbon also holds less electron density in the TS on the Ru_{57} (q_B = −0.34 e) than on the extended surface (q_B = −0.41 e), which reflects the increased energy barrier for CO cleavage on the site of the small NP (155 kJ mol^{-1}) compared to the extended surface (71 kJ mol^{-1}). In the case of B_5 $(104)_{2-2-1}$, a concave site, carbon's Bader charge is equivalent among the two systems (q_B = −0.40 and −0.38 e for Ru_{57} and the extended surface, respectively), also in agreement with the similar CO cleavage energy barrier (98 and 100 kJ mol^{-1}, respectively).

While Ru−O saturation-dependent stabilization may be expected for the concave sites, analogous to the case of adsorption, it may be surprising that the trend also holds for flat sites. This is because a CO molecule adsorbed in an η^1 geometry has to tilt and also form an η^2-coordinated TS for CO dissociation (TS structures in Figures S3 and S5). The pDOS and pCOHP curves for intermediate structures in between the adsorbed CO and the TS for its dissociation (extracted from the NEB) for the B_5 $(104)_{2-1-2}$ site (Figure S10) show indeed the formation of an η^2-bonded species whose electronic structure is very similar to that of CO adsorbed on a concave site, in which the Ru−O bonding extent is larger for the more saturated site of the large NP, as shown previously. In the case of flat sites, the Bader charge differences are smaller, though. For the B_5 $(100)_A$ site, for instance, C's charge is equal to −0.29 e on the Ru_{57} site (energy barrier of 214 kJ mol^{-1}) as compared to the extended surface site (q_B = −0.33 e, energy barrier of 174 kJ mol^{-1}). These results demonstrate that our rationale to understand CO activation using chemical bonding is actually general across the different types of step-edge sites.

4. CONCLUSION

In this work, we addressed the nature of CO adsorption and activation on Ru NPs of distinct sizes by means of first-principles calculations. We found that step-edge sites such as B_5 and B_6 sites can be accommodated in both smaller (1 nm) and larger (2 nm) Ru NPs, contrary to the assumption that they can only be formed on larger particles. Step-edges relevant for CO activation are among the most energetically favored defects formed on these NPs. The estimated energy required to form the most stable combination of B_5 sites is equal to 56 and 43 kJ mol^{-1} for Ru NPs of 1 and 2 nm size, respectively.

Two distinct types of step-edge sites were identified with respect to CO adsorption: *flat* and *concave*. While on flat sites CO adsorption geometry is typically η^1 normal to the surface analogously to sites in low-index surfaces, for concave sites we observe a preferential CO adsorption in a tilted η^2 geometry previously recognized experimentally on single-crystal surfaces as well as in molecular cluster organometallic analogues. As expected from bond order conservation, CO adsorption strength increases on flat sites of smaller NPs. However, the binding of CO is unexpectedly weaker on the concave sites of smaller NPs.

Using state-of-the-art crystal orbital Hamilton population analysis, we provide a molecular interpretation for CO bonding on concave step-edge sites of Ru NPs that allows rationalizing (i) the difference between the nature of CO adsorption on flat and concave sites as well as (ii) the unusual particle size effect on CO adsorption:

(i) For both flat and concave sites, the electron back-donation from the metal to the molecule is due to the population of a CO−metal *d* mixed band that contains

DOI: 10.1021/jacs.6b08697
J. Am. Chem. Soc. 2016, 138, 16655−16668

contributions from the 1π and $2\pi^*$ MOs of the CO molecule. Whereas for the CO η^1 adsorption on a flat site this band is localized in the oxygen atom of the CO molecule as an electron lone pair, the Ru−O interaction is able to distribute the electron density in the case of η^2 adsorption on a concave site, where both C and O atoms display equivalent contributions to the band. As a consequence of the electron delocalization, this band is stabilized and more populated below the Fermi level, being the electron back-donation much more effective for concave step-edge sites than for flat ones.

(ii) Concerning the particle size effect on CO adsorption, we conclude that σ donation increases the CO bonding on the less saturated flat sites present on small NPs, whereas the weakening of the Ru−O bond between the oxygen of the CO molecule and the surface reduces the back-bonding and thus the CO adsorption strength on concave sites of smaller Ru NPs. Therefore, there is a tendency for smaller NPs to favor η^1 adsorption compared to η^2. This bonding analysis is general within each category of sites and accounts for CO adsorption properties over a range of distinct step-edge sites with various geometries, such as B_5 or B_6 sites.

Regarding CO activation, we found that step-edge sites are much more reactive on larger NPs than on smaller ones. The lower reactivity of smaller NPs toward CO cleavage is therefore not due to the lack of step-edge sites, but rather to the higher energy barriers for CO cleavage on the less coordinated step-edges of small NPs. Furthermore, we show that thermodynamics, through the commonly used Brønsted−Evans−Polanyi relationships, fails to account for this effect, which can to be interpreted using CO bonding molecular models. The weaker Ru−O interaction that leads to less back-donation in the η^2 adsorbed state is also the origin for the higher CO direct cleavage energy barriers on step-edge sites of smaller NPs. The trend holds for both flat and concave types of sites, since in any case CO molecule has to be tilted to an η^2-bonded TS in order to dissociate.

The findings described in this contribution rationalize the observed particle size dependence of CO activation, showing how an electronic-structure-based molecular understanding combined with realistic catalysts models can be crucial in order to understand the activation of small molecules on the step-edge sites of metallic nanoparticles.

■ ASSOCIATED CONTENT

Supporting Information

The Supporting Information is available free of charge on the ACS Publications website at DOI: 10.1021/jacs.6b08697.

Further computational details and supplementary data, including Tables S1−S6 and Figures S1−S12 (PDF)

ESI optimized geometries (ZIP)

■ AUTHOR INFORMATION

Corresponding Author

*comas@inorg.chem.ethz.ch

ORCID

Aleix Comas-Vives: 0000-0002-7002-1582

Notes

The authors declare no competing financial interest.

■ ACKNOWLEDGMENTS

The authors thank the Swiss National Foundation (Ambizione project PZ00P2_148059), ETH (Research Grant ETH42 14-1), and SCCER Heat and Electricity Storage for financial support. The authors also acknowledge the Swiss National Supercomputing Center for providing computational resources (project s461).

■ REFERENCES

(1) Williams, W. D.; Shekhar, M.; Lee, W.-S.; Kispersky, V.; Delgass, W. N.; Ribeiro, F. H.; Kim, S. M.; Stach, E. A.; Miller, J. T.; Allard, L. F. *J. Am. Chem. Soc.* **2010**, *132*, 14018.

(2) Park, J. B.; Graciani, J.; Evans, J.; Stacchiola, D.; Senanayake, S. D.; Barrio, L.; Liu, P.; Sanz, J. F.; Hrbek, J.; Rodriguez, J. A. *J. Am. Chem. Soc.* **2010**, *132*, 356.

(3) Rofer-DePoorter, C. K. *Chem. Rev.* **1981**, *81*, 447.

(4) Khodakov, A. Y.; Chu, W.; Fongarland, P. *Chem. Rev.* **2007**, *107*, 1692.

(5) Xiao, C.-x.; Cai, Z.-p.; Wang, T.; Kou, Y.; Yan, N. *Angew. Chem.* **2008**, *120*, 758.

(6) den Breejen, J. P.; Radstake, P. B.; Bezemer, G. L.; Bitter, J. H.; Frøseth, V.; Holmen, A.; Jong, K. P. d. *J. Am. Chem. Soc.* **2009**, *131*, 7197.

(7) Filot, I. A. W.; van Santen, R. A.; Hensen, E. J. M. *Angew. Chem., Int. Ed.* **2014**, *53*, 12746.

(8) Blyholder, G. *J. Phys. Chem.* **1964**, *68*, 2772.

(9) Huheey, J. E.; Keiter, E. A.; Keiter, R. L.; Medhi, O. K. *Inorganic Chemistry: Principles of Structure and Reactivity*; Pearson Education: London, 2006.

(10) Föhlisch, A.; Nyberg, M.; Hasselström, J.; Karis, O.; Pettersson, L. G. M.; Nilsson, A. *Phys. Rev. Lett.* **2000**, *85*, 3309.

(11) Föhlisch, A.; Nyberg, M.; Bennich, P.; Triguero, L.; Hasselström, J.; Karis, O.; Pettersson, L. G. M.; Nilsson, A. *J. Chem. Phys.* **2000**, *112*, 1946.

(12) Dimakis, N.; Cowan, M.; Hanson, G.; Smotkin, E. S. *J. Phys. Chem. C* **2009**, *113*, 18730.

(13) Dimakis, N.; Navarro, N. E.; Mion, T.; Smotkin, E. S. *J. Phys. Chem. C* **2014**, *118*, 11711.

(14) Calle-Vallejo, F.; Loffreda, D.; Koper, M. T. M.; Sautet, P. *Nat. Chem.* **2015**, *7*, 403.

(15) Zubkov, T.; Morgan, G. A., Jr; Yates, J. T., Jr; Kühlert, O.; Lisowski, M.; Schillinger, R.; Fick, D.; Jänsch, H. J. *Surf. Sci.* **2003**, *526*, 57.

(16) Backus, E. H. G.; Eichler, A.; Grecea, M. L.; Kleyn, A. W.; Bonn, M. *J. Chem. Phys.* **2004**, *121*, 7946.

(17) Tison, Y.; Nielsen, K.; Mowbray, D. J.; Bech, L.; Holse, C.; Calle-Vallejo, F.; Andersen, K.; Mortensen, J. J.; Jacobsen, K. W.; Nielsen, J. H. *J. Phys. Chem. C* **2012**, *116*, 14350.

(18) Hammer, B. *Phys. Rev. Lett.* **1999**, *83*, 3681.

(19) Dahl, S.; Logadottir, A.; Egeberg, R. C.; Larsen, J. H.; Chorkendorff, I.; Törnqvist, E.; Nørskov, J. K. *Phys. Rev. Lett.* **1999**, *83*, 1814.

(20) Ciobica, I. M.; van Santen, R. A. *J. Phys. Chem. B* **2003**, *107*, 3808.

(21) Honkala, K.; Hellman, A.; Remediakis, I. N.; Logadottir, A.; Carlsson, A.; Dahl, S.; Christensen, C. H.; Nørskov, J. K. *Science* **2005**, *307*, 555.

(22) Ge, Q.; Neurock, M. *J. Phys. Chem. B* **2006**, *110*, 15368.

(23) Shetty, S.; Jansen, A. P. J.; van Santen, R. A. *J. Phys. Chem. C* **2008**, *112*, 14027.

(24) Shetty, S.; Jansen, A. P. J.; van Santen, R. A. *J. Am. Chem. Soc.* **2009**, *131*, 12874.

(25) Shetty, S.; van Santen, R. A. *Phys. Chem. Chem. Phys.* **2010**, *12*, 6330.

(26) Weststrate, C. J.; van Helden, P.; van de Loosdrecht, J.; Niemantsverdriet, J. W. *Surf. Sci.* **2016**, *648*, 60.

(27) van Hardeveld, R.; van Montfoort, A. *Surf. Sci.* **1966**, *4*, 396.

(28) Van Hardeveld, R.; Van Montfoort, A. *Surf. Sci.* **1969**, *17*, 90.

DOI: 10.1021/jacs.6b08697
J. Am. Chem. Soc. 2016, 138, 16655−16668

(29) Van Hardeveld, R.; Hartog, F. *Surf. Sci.* **1969**, *15*, 189.
(30) van Santen, R. A.; Neurock, M. *Molecular Heterogeneous Catalysis: A Conceptual and Computational Approach*; Wiley: Weinheim, 2009.
(31) García-García, F. R.; Guerrero-Ruiz, A.; Rodríguez-Ramos, I. *Top. Catal.* **2009**, *52*, 758.
(32) van Helden, P.; Ciobîcă, I. M.; Coetzer, R. L. J. *Catal. Today* **2016**, *261*, 48.
(33) Ligthart, D. A. J. M.; Filot, I. A. W.; Almutairi, A. A. H.; Hensen, E. J. M. *Catal. Commun.* **2016**, *77*, 5.
(34) Vilé, G.; Baudouin, D.; Remediakis, I. N.; Copéret, C.; López, N.; Pérez-Ramírez, J. *ChemCatChem* **2013**, *5*, 3750.
(35) Carballo, J. M. G.; Yang, J.; Holmen, A.; García-Rodríguez, S.; Rojas, S.; Ojeda, M.; Fierro, J. L. G. *J. Catal.* **2011**, *284*, 102.
(36) Quek, X.-Y.; Filot, I. A. W.; Pestman, R.; van Santen, R. A.; Petkov, V.; Hensen, E. J. M. *Chem. Commun.* **2014**, *50*, 6005.
(37) González-Carballo, J. M.; Pérez-Alonso, F. J.; Ojeda, M.; García-García, F. J.; Fierro, J. L. G.; Rojas, S. *ChemCatChem* **2014**, *6*, 2084.
(38) Loveless, B. T.; Buda, C.; Neurock, M.; Iglesia, E. *J. Am. Chem. Soc.* **2013**, *135*, 6107.
(39) Shetty, S.; van Santen, R. A. *Catal. Today* **2011**, *171*, 168.
(40) Kresse, G.; Hafner, J. *Phys. Rev. B: Condens. Matter Mater. Phys.* **1994**, *49*, 14251.
(41) Kresse, G.; Hafner, J. *Phys. Rev. B: Condens. Matter Mater. Phys.* **1993**, *47*, 558.
(42) Kresse, G.; Furthmüller, J. *Comput. Mater. Sci.* **1996**, *6*, 15.
(43) Perdew, J. P.; Burke, K.; Ernzerhof, M. *Phys. Rev. Lett.* **1996**, *77*, 3865.
(44) Perdew, J. P.; Burke, K.; Ernzerhof, M. *Phys. Rev. Lett.* **1997**, *78*, 1396.
(45) Maintz, S.; Deringer, V. L.; Tchougréeff, A. L.; Dronskowski, R. *J. Comput. Chem.* **2013**, *34*, 2557.
(46) Deringer, V. L.; Tchougréeff, A. L.; Dronskowski, R. *J. Phys. Chem. A* **2011**, *115*, 5461.
(47) Dronskowski, R.; Bloechl, P. E. *J. Phys. Chem.* **1993**, *97*, 8617.
(48) Hoffmann, R. *Solids and surfaces: a chemist's view of bonding in extended structures*; VCH Publishers: Weinheim, 1988.
(49) Hughbanks, T.; Hoffmann, R. *J. Am. Chem. Soc.* **1983**, *105*, 3528.
(50) Comas-Vives, A.; Furman, K.; Gajan, D.; Akatay, M. C.; Lesage, A.; Ribeiro, F. H.; Coperet, C. *Phys. Chem. Chem. Phys.* **2016**, *18*, 1969.
(51) Zhang, X.-Q.; Iype, E.; Nedea, S. V.; Jansen, A. P. J.; Szyja, B. M.; Hensen, E. J. M.; van Santen, R. A. *J. Phys. Chem. C* **2014**, *118*, 6882.
(52) Wellendorff, J.; Silbaugh, T. L.; Garcia-Pintos, D.; Nørskov, J. K.; Bligaard, T.; Studt, F.; Campbell, C. T. *Surf. Sci.* **2015**, *640*, 36.
(53) Blake, A. J.; Dyson, P. J.; Ingham, S. L.; Johnson, B. F. G.; Martin, C. M. *Inorg. Chim. Acta* **1995**, *240*, 29.
(54) Ingham, S. L.; Johnson, B. F. G.; Martin, C. M.; Parker, D. *J. Chem. Soc., Chem. Commun.* **1995**, *0*, 159.
(55) Zaera, F.; Kollin, E.; Gland, J. L. *Chem. Phys. Lett.* **1985**, *121*, 464.
(56) Moon, D. W.; Cameron, S.; Zaera, F.; Eberhardt, W.; Carr, R.; Bernasek, S. L.; Gland, J. L.; Dwyer, D. J. *Surf. Sci.* **1987**, *180*, L123.
(57) Shinn, N. D.; Madey, T. E. *Phys. Rev. Lett.* **1985**, *54*, 852.
(58) Hoffmann, F. M.; de Paola, R. A. *Phys. Rev. Lett.* **1984**, *52*, 1697.
(59) Shinn, N. D.; Trenary, M.; McClellan, M. R.; McFeely, F. R. *J. Chem. Phys.* **1981**, *75*, 3142.
(60) Filot, I. A. W.; Shetty, S. G.; Hensen, E. J. M.; van Santen, R. A. *J. Phys. Chem. C* **2011**, *115*, 14204.
(61) Melander, M.; Latsa, V.; Laasonen, K. *J. Chem. Phys.* **2013**, *139*, 164320.
(62) Nandula, A.; Trinh, Q. T.; Saeys, M.; Alexandrova, A. N. *Angew. Chem., Int. Ed.* **2015**, *54*, 5312.
(63) Cusinato, L.; Martinez-Prieto, L. M.; Chaudret, B.; del Rosal, I.; Poteau, R. *Nanoscale* **2016**, *8*, 10974.
(64) Hibbitts, D. D.; Loveless, B. T.; Neurock, M.; Iglesia, E. *Angew. Chem., Int. Ed.* **2013**, *52*, 12273.
(65) Hibbitts, D.; Dybeck, E.; Lawlor, T.; Neurock, M.; Iglesia, E. *J. Catal.* **2016**, *337*, 91.
(66) Hibbitts, D.; Iglesia, E. *Acc. Chem. Res.* **2015**, *48*, 1254.
(67) Kresse, G.; Gil, A.; Sautet, P. *Phys. Rev. B: Condens. Matter Mater. Phys.* **2003**, *68*, 073401.
(68) Filot, I. A. W.; Fariduddin, F.; Broos, R. J. P.; Zijlstra, B.; Hensen, E. J. M. *Catal. Today* **2016**, *275*, 111.

NOTE ADDED AFTER ASAP PUBLICATION

ESI optimized geometries (ZIP) were added and Figure 1 was corrected on December 28, 2016.

DOI: 10.1021/jacs.6b08697
J. Am. Chem. Soc. 2016, 138, 16655−16668